

Sensitivity and Backgrounds of Phase-I and II of the COMET Experiment

Benjamin Edward Krikler
of Imperial College London

A dissertation submitted to Imperial College London
for the degree of Doctor of Philosophy

Abstract

Declaration

This dissertation is the result of my own work, except where explicit reference is made to the work of others, and has not been submitted for another qualification to this or any other university. This dissertation does not exceed the word limit for the respective Degree Committee.

Benjamin Edward Krikler

Acknowledgements

Contents

1. Theory	2
2. The COMET Experiment	3
2.1. Overview of Signal and Backgrounds	4
2.2. General Experimental Techniques	6
2.2.1. Proton Beam Energy and Production Target	6
2.2.2. Particle Transport through Bent Solenoids	7
2.2.3. Stopping Target Material and Beam Pulsing	10
2.3. COMET Phase-I	14
2.4. COMET Phase-II	15
2.5. Schedule and Status	17
3. Offline Software and The COMET Simulation	21
3.1. Developing the COMET Offline Framework	21
3.2. Overview of ICEDUST	24
3.3. The COMET Simulation	26
3.3.1. Handling Geometry	27
3.3.2. Field Calculation	27
3.3.3. Production Target Simulations	27
3.3.4. Extending the Geant4 Physics Modelling	27
3.3.5. Resampling With the Hit Merger	27
4. Phase-II Optimisation	28
4.1. Optimisation Strategy	29
4.2. Optimisation Goals	30
4.3. Production Target Optimisation	30
4.3.1. Configuration	30
4.3.2. Length Scan	32
4.3.3. Radius scan	34

4.3.4. Final Result	34
5. Phase-II Signal Sensitivity	37
6. Phase-II Backgrounds	38
A. Drifts in a Bent Solenoid	39
A.1. Uniform Solenoidal Field	39
A.2. Field in a Bent Solenoid	39
A.3. Drift Calculation	40
A.3.1. Gradient Drift	40
List of Acronyms	43
Bibliography	44

Chapter 1.

Theory

Chapter 2.

The COMET Experiment

The aim of the COMET experiment is to search for COherent Muon to Electron Transitions with a single-event-sensitivity of around 3×10^{-17} . This amounts to an improvement of four orders of magnitude compared to the current limit [9] which requires some significant changes to the way the experiment operates.

The general experimental goals of COMET are to:

- stop many muons in aluminium,
- have a high signal acceptance,
- suppress potential background sources to well below a single event.

At the level of sensitivity desired for COMET these requirements translate to the need for:

- a very high intensity muon beam,
- a thin stopping target and low material budget detector,
- a low energy muon beam,
- a pulse beam and relatively low-Z stopping target.

Realising these goals requires many new experimental techniques and as such COMET has decided to operate in two stages, Phase-I and Phase-II. Phase-II will realise the final objective of 3×10^{-17} , whilst Phase-I aims for a measurement with sensitivity of 3×10^{-15} but also to understand the beam and backgrounds to improve our understanding of Phase-II. In order to understand both phases a simple appreciation of the types of backgrounds that must be considered is valuable, so I shall first give an overview of these.

Type	Background	Predicted number of events during run	
		Phase-I [21]	Phase-II [10]
Intrinsic	Muon Decay-in-Orbit	0.01	0.15
	Radiative Muon Capture	0.0019	< 0.001
	μ^- Capture w/ n Emission	< 0.001	< 0.001
	μ^- Capture w/ Charged Part. Emission	< 0.001	< 0.001
Prompt	Radiative Pion Capture	0.00028	0.05
	Beam Electrons		< 0.1*
	Muon Decay in Flight	≤ 0.0038	< 0.0002
	Pion Decay in Flight		< 0.0001
	Neutron Induced	$\sim 10^{-9}$	0.024
Delayed	Delayed Radiative Pion Capture	~ 0	0.002
	Anti-proton Induced	0.0012	0.007
	Other delayed B.G.	~ 0	—
Cosmic	Cosmic Ray Muons	—	0.002
	Electrons from Cosmic Ray Muons	< 0.01	0.002
Total background		< 0.032	< 0.34
Signal (Assuming $B = 1 \times 10^{-16}$)		0.31	3.8

Table 2.1.: Backgrounds for COMET Phase-I [21] and Phase-II [10]. Prompt backgrounds arise by protons that occur in between bunches and are therefore suppressed by the extinction factor. For Phase-I, the recently measured value of 10^{-12} was used for the extinction factor, but for Phase-II the older expectation of 10^{-9} was used. If this is not taken into account, the Phase-I estimates suggest a greater background to signal sensitivity than for Phase-II. *) Result was statistically limited.

2.1. Overview of Signal and Backgrounds

μ - e conversion is experimentally attractive because its signal is so simple: a single monoenergetic electron at close to the muon mass of 105 MeV/c, given by:

$$E_e = M_\mu - E_{\mu, \text{binding}} - E_{\text{recoil}} \quad (2.1)$$

where $M_\mu = 105.66$ MeV/c² is the muon mass, $E_{\mu, \text{binding}}$ the binding energy of the muon in the ground state of the muonic atom, and E_{recoil} is the kinetic energy of the recoiling

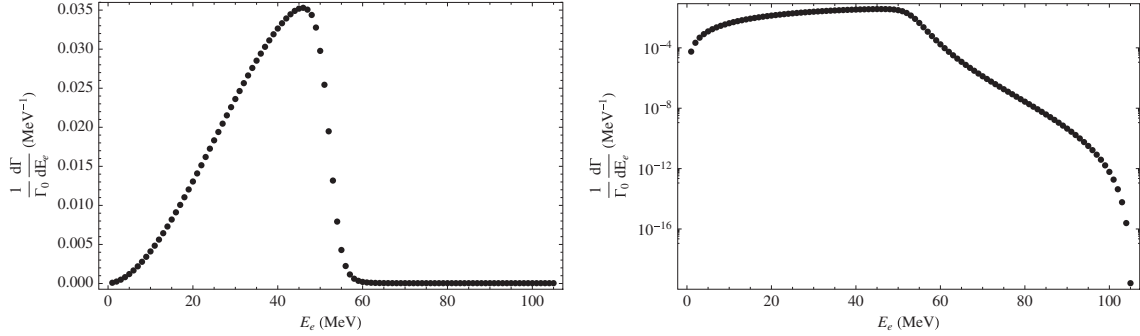


Figure 2.1.: Spectrum of electrons coming from muon decay-in-orbit by Czarnecki et al. [12]. The two spectra are the same, but left is on a linear-linear scale whilst the right plot is on a log-lin scale which shows clearly the high-energy tail reaching up to the μ - e conversion signal energy of 105 MeV.

nucleus. In the aluminium target used for COMET (see section 2.2.3) the electron energy is $E_e = 104.97$ MeV.

Background rates must be kept well below the signal sensitivity if an observation is to be confidently identified as signal, or if meaningful limits are to be set. Given the desired sensitivity of COMET is 3×10^{-15} at Phase-I and 3×10^{-17} by Phase-II, background rates must be kept equally rare.

Table 2.1 summarizes the results of previous studies for background rates at Phase-I and Phase-II. There are predominantly four main groups of background sources: intrinsic, prompt, delayed and cosmic sources.

Intrinsic processes are those that arise from muons stopping in the target and will therefore always be present regardless of how well you make your muon beam and detector. Of these, the dominant background is muon decay in orbit (DIO), which is the standard model process of a muon decaying to an electron, emitting two neutrinos in the process. Although the decay of a free muon cannot produce electrons with energy greater than half the muon mass, once bound to a nucleus the neutrinos can be configured to carry almost no kinetic energy away, such that only the nucleus and electron are important in the end-point configuration. It can immediately be seen then the kinematics of the end-point configuration for muon decay-in-orbit are the same as for μ - e conversion, and indeed a tail in the spectrum of electrons coming from muon DIO extends all the way up to this point. Fig. 2.1 shows the spectrum of electrons from muon DIO in aluminium where it can be seen that the high energy tail does reach up to about 105 MeV/c, but with a very steeply falling rate.

Delayed and prompt processes can come from impurities in the muon beam, the key difference being the timing with respect to the proton beam arrival. For example, pions reaching the stopping target region are dangerous since they can produce high energy gamma rays which can pair produce to create 105 MeV electrons. Since pion capture against a nucleus is extremely fast (less than 1 ns) the timing of pion-induced backgrounds is determined solely by the arrival time of pions into the target region. In order to reach this region without decaying, the pions must be relatively high momentum of about 60 MeV/c or greater. As a result, backgrounds from pion capture are typically expected close to the arrival of protons at the production target. These sort of prompt processes are suppressed by using a pulse proton beam (discussed in more depth later) and ensuring very few protons in between pulses. Should a pion in the beam arrive at the target region with a large delay then the timing of the proton beam is not a useful method for suppressing this. Possible causes of this against which must be mitigated is the mirroring of particles in the magnetic field or by production of pions and high-energy electrons from antiprotons. At a given momentum, antiprotons travel considerably more slowly than muons or pions given their considerably larger mass. Other beam related issues include the decay of muons and pions to electrons. An electron of 100 MeV/c can be produced by muons or pions with greater than 70 or 50 MeV/c respectively, and so the flux of higher energy particles must be removed.

Finally cosmic backgrounds arise from high energy muons that pass through the building and enter the detector or beamline. Events where a muon decays to an electron which is then detected as 105 MeV are counted as backgrounds. In particular, muons that produce high energy electrons close to the target are dangerous since cuts on the reconstructed direction and position will be less effective.

2.2. General Experimental Techniques

2.2.1. Proton Beam Energy and Production Target

The muon beam used in COMET is produced as the decay products of a secondary pion beam created by protons striking a target. If maximising the muon intensity were the only concern, then both the proton beam energy and atomic mass of the target material would also be maximised since the pion production cross section grows with

these two parameters. However, the need to suppress background rates and maintain the mechanical and operational stability of the target constrain both of these parameters.

In particular, protons with more than 5.6 GeV (*((CHECK: Target dependence? Correct?))*) striking a stationary target have sufficient energy to produce antiprotons which travel relatively slowly (see 2.2.3) and can produce backgrounds. Since the antiproton yield grows very quickly above this threshold, it has been chosen to use protons with 8 GeV kinetic energy.

For Phase-II running, the main ring will operate at 7 μA so that a beam power of 56 kW is achieved. Phase-I on the other hand will use a lower beam intensity of 0.4 μA or 3.2 kW.

A heavy metal target is preferable since it improves the pion yield, in particular tungsten since it is relatively cheap compared to other options. However, at the beam powers under consideration, a metal target would melt, such that we must actively cool the target. Such will be the approach in Phase-II, however for simplicity Phase-I will run with a radiatively cooled graphite target.

((CHECK: Figure for pion vs. antiproton production cross-section for different proton energies and/or target materials))

Finally, only those pions and muons emitted in the backwards direction with respect to the proton beam are captured and transported to the muon beamline. This is a strong way to reduce the high-energy components of the muons and pions distributions since the yield for low momentum pions in the forward and backwards direction is similar, whilst the high energy tail is greatly suppressed in the backwards direction. At this time however, there is a dearth of experimental measurements for pion production in the backwards direction with 8 GeV protons on a graphite or tungsten target. Fig. 2.2 shows a measurement of the cross section for pion production with 10 GeV protons on tantalum (which is adjacent to tungsten on the periodic table).

2.2.2. Particle Transport through Bent Solenoids

Both Phase-I and II make use of bent solenoids to help select particles of a particular momentum. In bent solenoids, a dispersion occurs that is proportional to the momentum and charge of the particle passing through it.

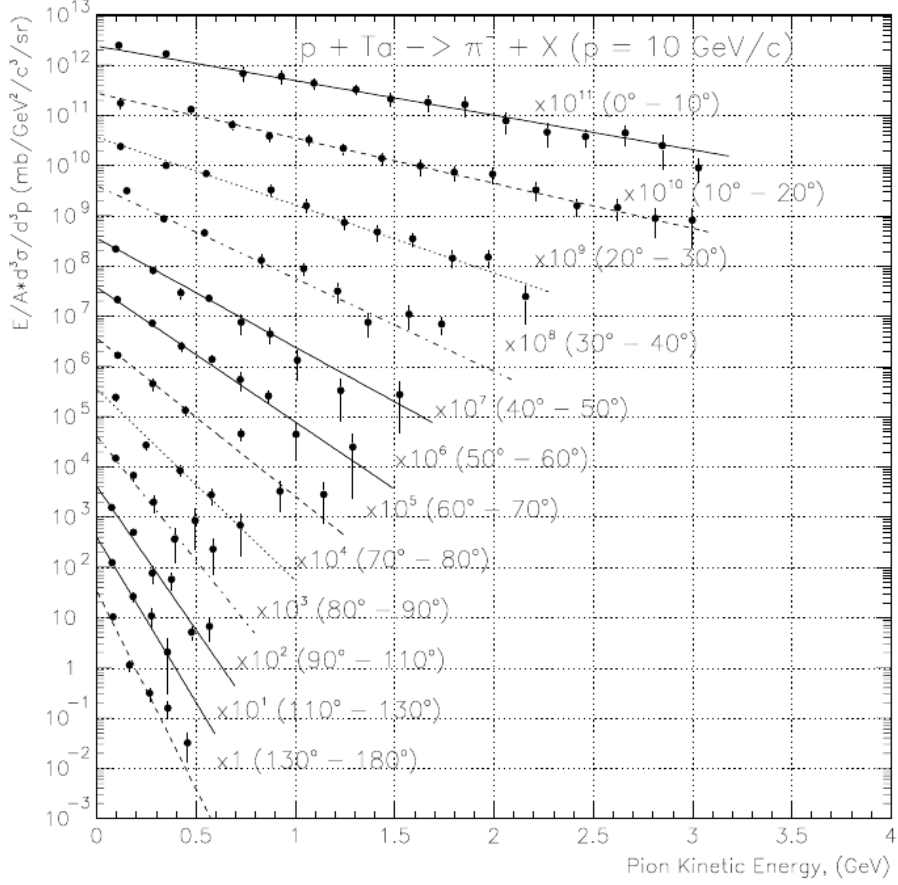


Figure 2.2.: Double differential cross section of pion production on a tantalum target from protons with 10 GeV kinetic energy (reproduced from Meco note 23 [13] which itself used [7]). It is clear that the high-energy component of the spectrum is suppressed as you move to higher production angles which is important for reducing background rates.

Charged particles moving through a straight solenoid follow a helical trajectory, orbiting a point that moves parallel to the solenoidal axis with constant velocity fixed by the longitudinal momentum of the particle. The frequency that the particle rotates about this point (betatron frequency or frequency of gyration) is determined by the transverse momentum.

By comparison, if a charged particle moves through a solenoid channel that has been bent, the particle can still be considered to orbit a point, only now the motion of that point can be shown to drift vertically, out of the plane of bending. This drift arises from the gradient introduced to the field by bending the solenoid but also from the non-rectilinear coordinate system of the field lines. The total drift, D , of a particle with mass and charge m and q respectively through a solenoid bent with a fixed radius of

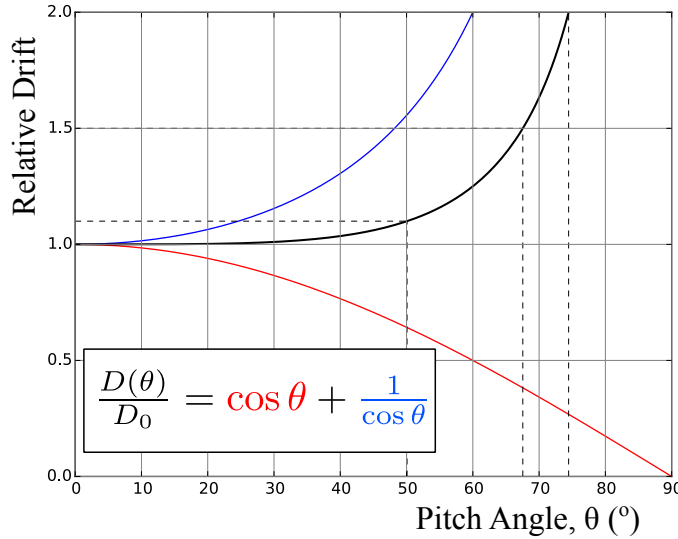


Figure 2.3.: Angular dependence of the magnitude of vertical drift in a bent solenoid field. The total variation (black) remains below 10% for pitch angles below 50°.

curvature, R , is given by:

$$D = \frac{1}{qB} \left(\frac{s}{R} \right) \frac{p_L^2 + 0.5p_T^2}{p_L} \quad (2.2)$$

$$= \frac{1}{qB} \left(\frac{s}{R} \right) \frac{p}{2} \left(\cos \theta + \frac{1}{\cos \theta} \right) \quad (2.3)$$

where B is the magnetic field strength¹, s is the distance travelled through the solenoid, p the momentum of the particle, with longitudinal and transverse components with respect to the solenoid axis, p_L and p_T respectively. The pitch angle, θ , is a property of the helical trajectory taken by the particle and defined as:

$$\theta = \tan^{-1} \left(\frac{p_T}{p_L} \right) \quad (2.4)$$

See Appendix A for a derivation of equations (2.2) and (2.3). The angular dependence of this equation is shown in Fig. 2.3 where it can be seen that for angles below 50 degrees the variation in the drift is less than 10%, such that the drift is determined almost completely by the momentum of particles up to these angles.

¹Strictly speaking, B is the field strength along the path of the centre of gyration, which is constant for a fixed transverse distance from the focus of the bent solenoid.

Bent solenoids are used to disperse high-energy muons and pions in the muon beam for both Phase-I and II, and as a spectrometer system for electrons coming from the stopping target in Phase-II, which will both be described in more detail below.

Since the drift is proportional to the momentum of the particle, those particles with zero momentum would remain on axis, whilst particles of interest (105 MeV electrons in the Phase-II electron spectrometer and around 40 MeV/c muons in the muon beam line) drift to the sides. To overcome this issue, a vertical component to the field lines is introduced. If the solenoid were straight the axis of a particle's helical trajectory would follow the field line. A vertical component would therefore cause the trajectories to move upwards with the field line itself. The same result is true in a bent solenoid and since the drift this introduces is not proportional to momentum a vertical component can be used to select at which momentum particles remain on-axis. Two techniques have been considered to introduce this vertical component: tilting the solenoid coils themselves, or adding additional dipole coils around the solenoids. COMET has opted to pursue the latter, using a special, proprietary winding technique developed by Toshiba to introduce a vertical component by placing additional conductor around the other solenoid coils. Since the current through these dipole coils can be altered separately to the solenoid coils, this approach has the advantage that the two can be tuned against the other so that the optimal dipole field can be found whilst running and or the acceptance can be shifted to another momentum or charge to study backgrounds. Additional collimator material can also be introduced to remove particles with undesirable momentum.

2.2.3. Stopping Target Material and Beam Pulsing

The combination of using backwards going pions and the long, bent-solenoid transport channel is already effective at removing potential background issues. In addition to these however, there is one further method which helps both to reduce beam-related backgrounds and improve the detector occupancy and reconstruction requirements: the use of a pulsed proton beam with a relatively light stopping target.

Since the signal process is coherent, its cross section grows roughly as the square of the number of nucleons (or protons, depending on the model)² until the muon is contained almost completely within the nucleus at which point the rate levels off. It is therefore desirable to use a high-Z target in order to increase the probability of conversion

²Although this growth is offset by the normalisation to the capture rate which is incoherent and grows linearly with the number of nucleons, so that the conversion rate itself is roughly linear.

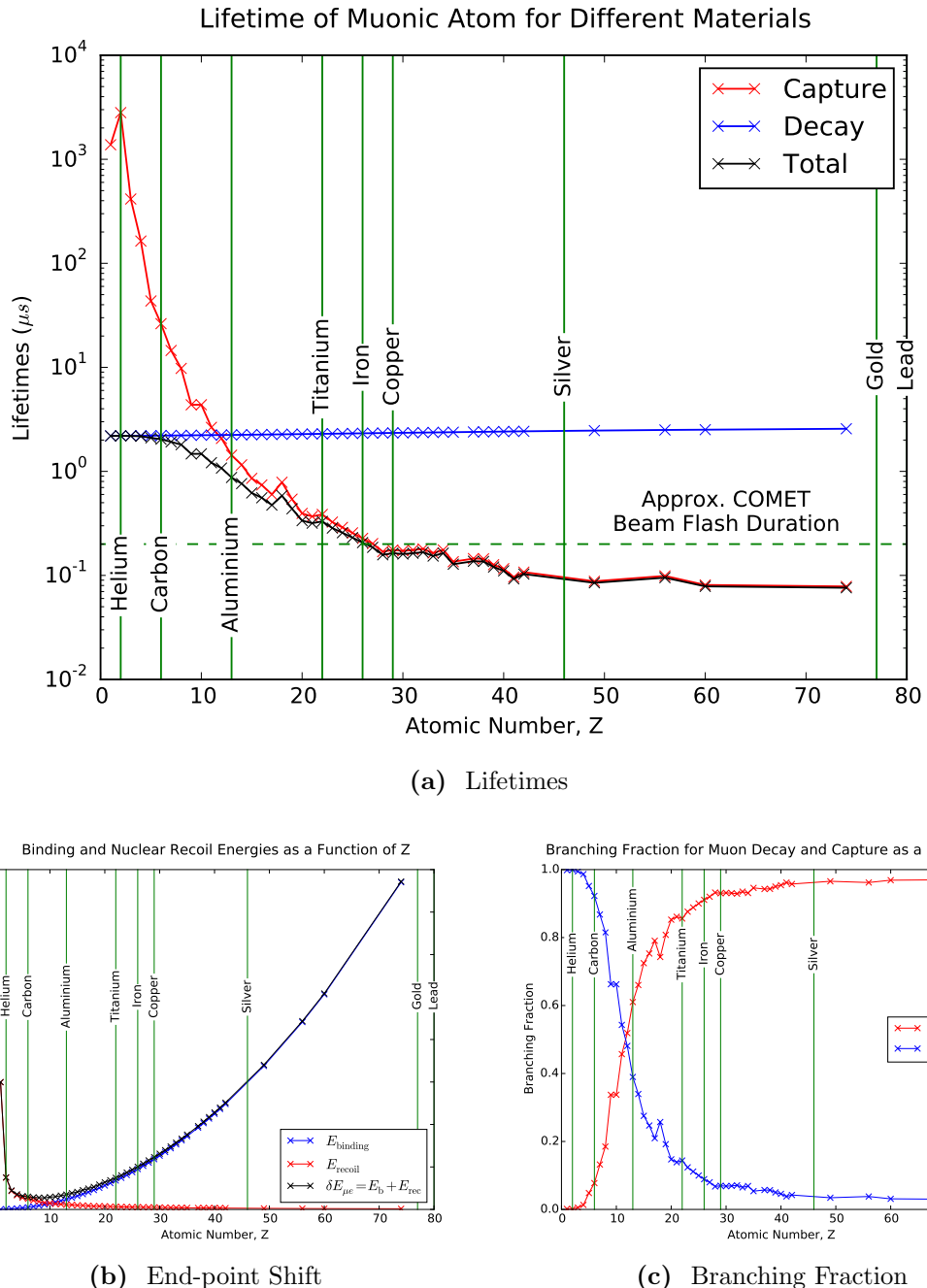


Figure 2.4.: The effect of changing the atomic number on the branching ratio, lifetime and electron energy spectrum end-point. For the branching ratio and lifetime plots, the partial rate for muon nuclear capture and decay-in-orbit are shown separately. The capture and decay rates are taken from the Geant4 [6] parametrisation for stopped negative muons. Only elements for which at least 1 isotope uses a measured value are plotted. The values for the end-point energy level are calculated using the Bohr model for the muon ground-state binding energy.

and indeed SINDRUM-II used both lead and gold targets, with its most stringent limit coming on gold [9].

However, as the nucleus gets larger, the lifetime of the muonic atom falls steeply due to the increase in the nuclear capture rate. This is illustrated in Fig. 2.4 where it can be seen that for elements heavier than iron ($Z > 26$) the muon lifetime is less than 200 ns. The COMET beamline produces a beam flash that lasts for about 200 ns after the arrival of a proton at the production target. This means that for targets heavier than iron timing information can not be used to distinguish particles coming from the beam or from the decay of a muon stopped in the target.

Whilst these are the two dominant factors in deciding the target material, other factors like the mechanical stability, cost, isotopic purity and the stability of the daughter nuclei following muon capture on the target must also be considered. Accordingly, titanium and aluminium are considered the two most viable target materials. Titanium, in which the muon lifetime is about 330 ns, would be considerably harder to measure μ - e conversion so at this stage the COMET experiment is focussed on using aluminium where the muon lifetime is about 864 ns [20].

The J-PARC accelerator has buckets separated by 550 ns, although separations of multiples of this number can in principle be achieved. For COMET running the intention is to fill every other bucket so that a separation of 1.17 μ s is achieved. Fig. ?? shows the beam timing schematically. A window from about 700 to 1100 ns after the proton beam arrival is then used to look for signal events, by which time most of the beam flash should have passed whilst signal events remain probable.

Having a well-defined bunch structure is crucial for this scheme to work. Protons arriving in between bunches would produce (a fragment of) beam flash that could include high energy muons or pions which could result in background electrons arriving within the timing window. The extinction factor quantifies the chance of this and is given by:

$$R_{\text{Extinction}} = \frac{N(p \text{ between bunches})}{N(p \text{ per bunch})} \quad (2.5)$$

Original estimates were made assuming $R_{\text{Extinction}}$ was around 10^{-9} [10] (about 1 out-of-time proton for every 7 bunches) although recent measurements have been able to demonstrate extinction at a level of 10^{-12} [?] (about 1 out-of-time proton for every 7100 bunches).

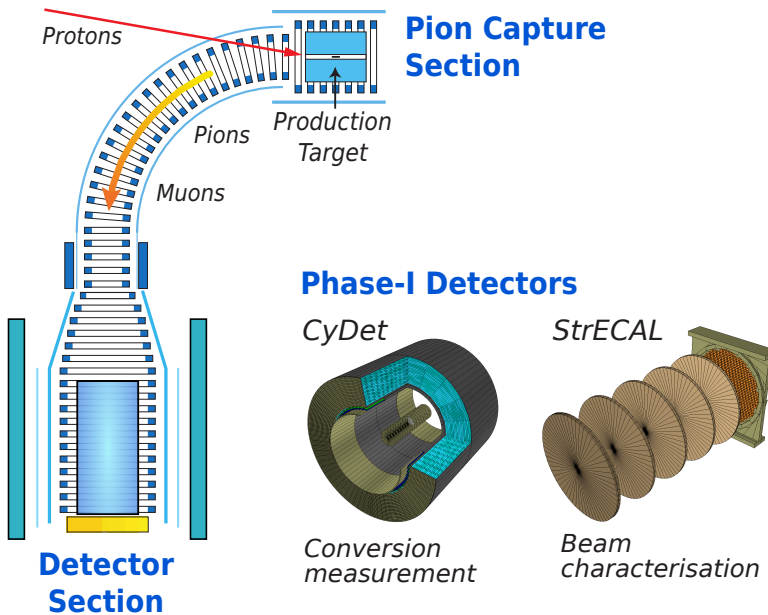


Figure 2.5.: Schematic layout of COMET Phase-I.

The bunch structure is initially defined by the linac at J-PARC which accelerates protons up to 600 MeV. The J-PARC Rapid Cycling Synchrotron ([RCS](#)) then takes these protons up to 3 GeV where up to two buckets can be stored at a time, although for COMET only one bunch at a time will be filled. The protons are then injected into the J-PARC Main Ring ([MR](#)) which accelerates them up the final energy of 8 GeV and is capable of storing up to 9 buckets at once. Using the Linac chopper alone would not be sufficient to keep the extinction factor since stray protons tend to drift into the unfilled buckets. Achieving the high extinction factor then is possible only by using the injection kicker from the [RCS](#) to the [MR](#) in a ‘double-kick’ mode. The kicker excitation length is set to two buckets (so that the [RCS](#) is completely emptied into the [MR](#)). The kicker is then activated again immediately after the first filled bunch has performed a complete rotation of the [MR](#) such that protons that had diffused into the second bunch of the [RCS](#) are now kicked away. Thus only four out of the nine buckets in the [MR](#) are filled and all other buckets are kept empty.

2.3. COMET Phase-I

Phase-I will see the construction of the COMET hall, the production target capture solenoids, the first 90 degrees of the bent muon transport solenoid, and the detector solenoid. The beamline is shown schematically in Fig. 2.5 where the two interchangeable detector systems can also be seen.

There are two key goals to Phase-I:

1. measure μ - e conversion at a sensitivity of 3×10^{-15} ,
2. prepare for Phase-II by measuring the beam profile, particle yields and background rates, and prototype the detector technology.

Since the dynamics of bent solenoids are complicated, it is important to study the beam as close to the production target as possible. However, due to the high radiation environment, it is important that the detector and electronics be kept well shielded. Phase-I will therefore measure the beam after the first 90 degrees of bent solenoid using the same detector system to be used in Phase-II, namely the Straw tube tracker and Electromagnetic Calorimeter ([StrECAL](#)) detector – a series of Straw Tracker stations followed by an ECAL all sitting in the beam.

However, since the StrECAL detector will be hit by the full force of the muon beam, it would not be feasible to conduct a μ - e conversion search using this detector. As such, for Phase-I a second detector, known as the Cylindrical Detector ([CyDet](#)) will be used for this purpose. The [CyDet](#) uses a Cylindrical Drift Chamber to reconstruct the trajectories of charged particles and a pair of Cherenkov and Scintillation counters (one upstream and one down) to trigger the read-out of the system. The [CyDet](#) escapes the issue of the beam flash that the [StrECAL](#) would face at Phase-I since only the outer region is instrumented. Since the detector sits in a 1 T solenoid field (and both the detector and solenoid are co-axial), particles follow helical trajectories with the radius of gyration determined by the transverse momentum of the particle. The beam is introduced in the centre and typically remains in an envelope of 15 cm whilst the stopping target sits in the centre of the detector with a radius of 10 cm. As such the detector itself is geometrically blind to charged particles in the beam and electrons coming from muon [DIO](#) in the target with momentum less than 60 MeV/c which make up the majority of the [DIO](#) spectrum. To reconstruct the longitudinal position of the particle’s trajectory an all-sereo configuration is used in the Cylindrical Drift Chamber, where each layer is

rotated in the opposite direction compared to the previous layer by an angle of 4° with respect to the solenoid axis.

Because the Phase-I detector sits much closer to the stopping target, there is greater exposure to hadrons emitted following nuclear capture of the stopped negative muons, such as protons, deuterons, alpha particles and so on. Despite being emitted with kinetic energies of a few tens of MeV, momenta above 60 MeV are readily achieved given the large mass of these particles. For similar reasons these particles are typically very heavily ionising, so if left unchecked could readily dominate the occupancy of the Cylindrical Drift Chamber ([CDC](#)). The AlCap experiment has shown that for muon capture on Al-27 nuclei, the emission of a proton occurs for about 3% of every muon capture [22]. At this level, it is believed that no specific shielding is required beyond the carbon inner wall of the [CDC](#) needed to contain the gas mixture.

Four layers of scintillation bars will surround the outside of the detector to provide a veto for cosmic ray events. The most dangerous event would be a high energy muon reaching the target and decaying to a 105 MeV electron which is then detected. Dedicated cosmic runs will be performed prior to operation with a beam in order to understand the flux of cosmic muons. Since the neutron flux from

2.4. COMET Phase-II

Since chapter 4 presents an in-depth optimisation of the design of Phase-II, I shall only give a brief introductory overview here, most of which is based on the design as laid out in the CDR [10].

COMET Phase-II will be the final stage of the experiment. It will extend the muon beamline built in for Phase-I by an extra 90° , and add two extra solenoid sections: one to hold the stopping target, and a second 180° bent solenoid with a large aperture of 60 cm radius. This layout is shown in Fig. 2.6. The bent solenoid after the stopping target acts both as a spectrometer, but also to remove the low energy [DIO](#) electrons which otherwise could significantly increase the hit rate in the detector. The final detector system for Phase-II will use the [StrECAL](#) from Phase-I but probably with thinner diameter straw tubes, thinner straw material, and more tracking stations in order to improve the energy resolution.

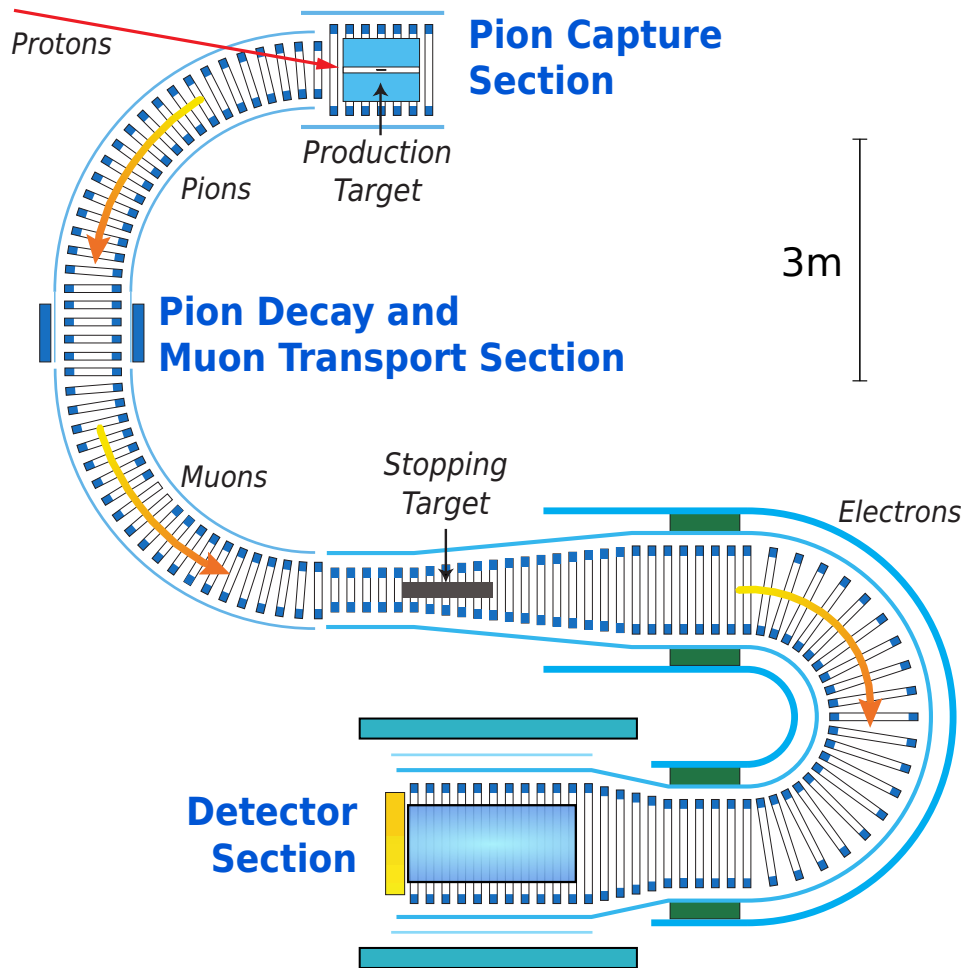


Figure 2.6.: Schematic layout of COMET Phase-II. The 8 GeV proton beam enters from the top-left, producing (amongst other things) pions. Pions and muons travelling backwards with respect to the proton beam are then transported around 180 degrees of bent solenoid, during which time most of the pions decay producing an intense muon beam. About 40% of these muons then stop in the stopping target (centre of image). Any electrons coming from μ - e conversion are then transported through another 180 degrees of bent solenoid into the detector system.

The stopping target itself has typically been designed as thin disks of aluminium, followed by a beam blocker. Even including the growth of the beam envelope as it passes from the 3 T field in the bent muon transport solenoids to the 1 T of the bent electron spectrometer solenoid the beam blocker removes all line-of-sight between the entrance of the electron spectrometer and the muon transport solenoids so that most of the beam flash is prevented from reaching the detector. The tapering of the field occurs almost

completely across the target itself with the intention that signal electrons heading initially upstream will be magnetically mirrored back towards the detector.

As for Phase-I, an active cosmic ray veto will prevent triggering on events caused by cosmic muons. At least the detector solenoid will be covered, but there is some scope

2.5. Schedule and Status

The overall schedule for the COMET experiment is shown in Fig. 2.7. Phase-I is due to start data taking in Japanese Fiscal Year ([JFY](#)) 2018 so that construction and development is well underway.

At the time of writing, with regards to the facility, the building to house the experiment is now finished attached to the side of the existing Hadron Hall at the Japanese Proton Accelerator Research Complex ([J-PARC](#)). Cooling and power supplies are being installed and the shielding for the concrete hatch area is being produced. In the mean time the development of the new beamline to extract protons from the [MR](#) and deliver them to the COMET area is being installed. In particular, the Lambertson magnet which directs the protons towards COMET rather than the existing Hadron Hall has been built. For the muon beamline, the Phase-I section of the bent muon transport solenoids has been built and installed and is now under commissioning studies. Construction of the detector solenoid has also begun with the capture solenoids around the production target

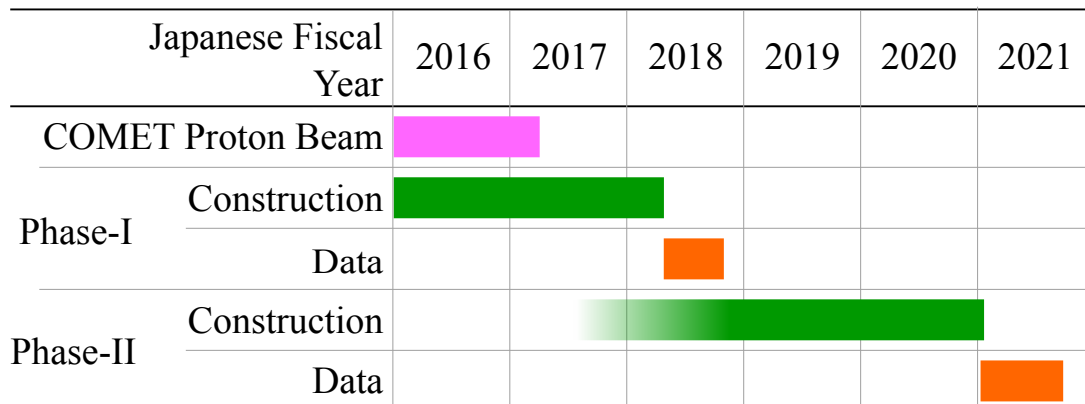


Figure 2.7.: A summarised timeline for the COMET experiment including Phase-I and Phase-II based on the 2016 TDR [21]. At the time of writing, construction of the detector solenoid is underway as well as the final stages of the facility.

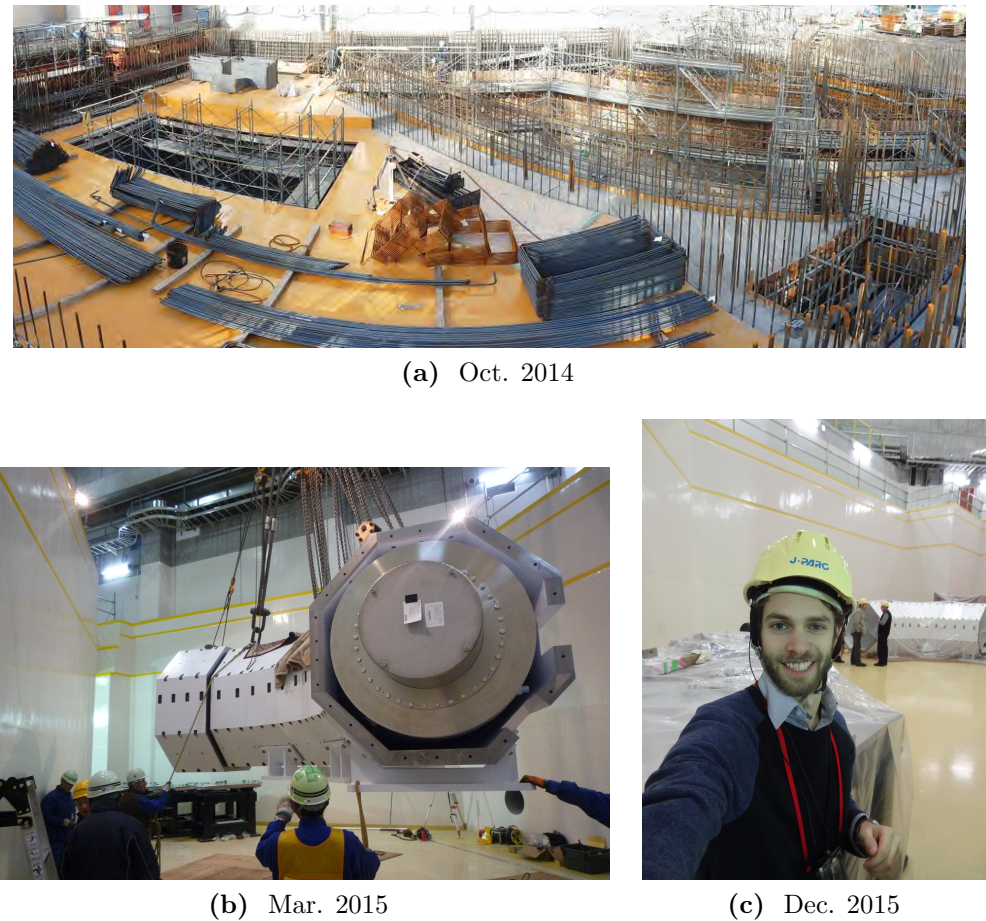


Figure 2.8.: Photographs of the experiment hall being constructed and first sections of beamline being installed.

soon to begin. A selection of photographs that show the construction of the facility and installation of the bent transport solenoid are show in Fig. 2.8.

Much of the recent activity for the collaboration has been on the design and construction of the detector systems. Beam tests to understand the performance and resolution of prototype ECAL crystals, straw tubes and the [CDC](#) have taken place. For the [StrECAL](#), production of all 2500 Phase-I straws has been completed and procurement of the Cerium-doped Lutetium Yttrium Oxyorthosilicate ([LYSO](#)) crystals for the ECAL is under way with some 200 or so crystals already purchased. Aging tests of the straw tubes are under way with straws under pressure and tension are being held for a long duration at KEK. Analysis of beam-test data is underway to understand the position resolution for a given straw, and the energy resolution of the ECAL, although better than 5% resolution for 105 MeV electrons has already been shown. Fig. 2.9 shows photographs of the prototypes and beam test set-ups of the Straw Tube Tracker and the ECAL.

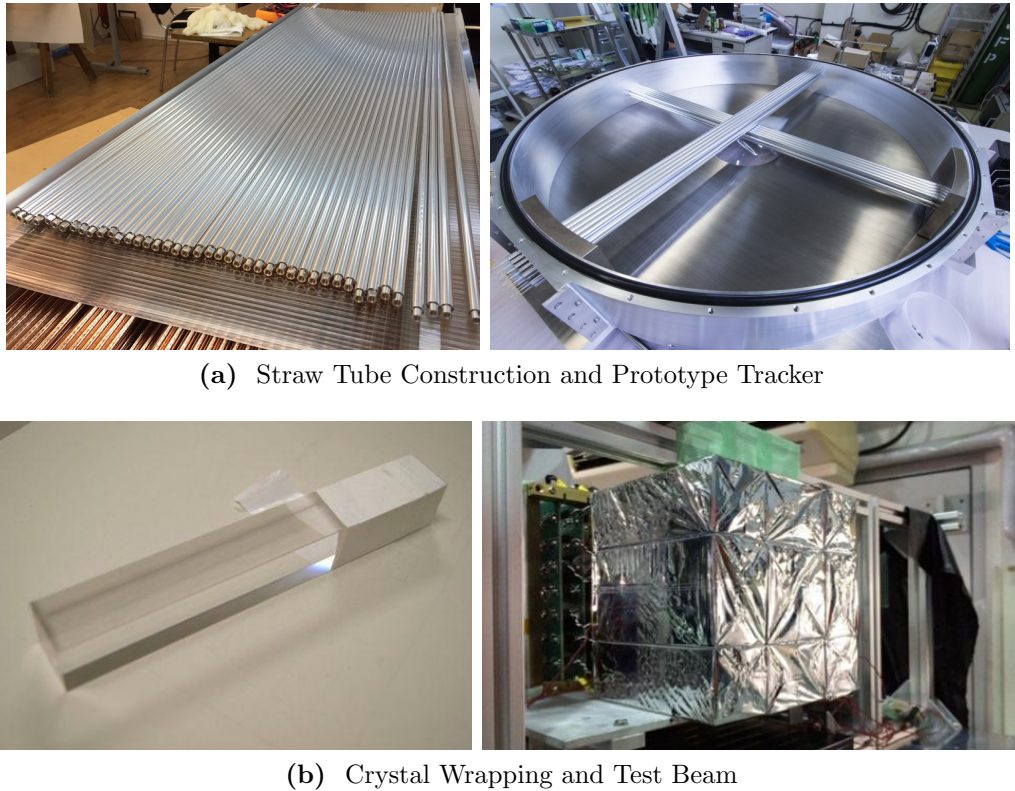


Figure 2.9.: Research and development for the [StrECAL](#) showing both the individual straws or crystal and a prototype set up used at test beams to characterise the sub-detectors.

In the meantime the full [CDC](#) has been strung, with some 20,000 wires less than 10 microns thick (*((CHECK: is this the correct wire size))*) being inserted. Every wire has had its tension checked using a vibrational resonance method, which showed some .. (*((CHECK: How many wires needed to be replaced))*) wires were too loose and have since been replaced. Currently the inner wall of the [CDC](#) is being inserted so that leak tests can begin shortly. Fig. 2.10 shows photographs from the stringing of the [CDC](#). In parallel, cosmic ray tests have been used to study to the performance of [CDC](#) prototypes and analysis of the data is under way to deduce the X-T curve for the [CDC](#) cells.

In the less-tangible realm that is software and simulation, in April last year the offline software reached its first stable release, and has since been used to perform three large-scale Monte Carlo productions of Phase-I. The most recent production saw the simulation of around 10^{10} Protons on Target ([POT](#)), equivalent to about 20,000 bunches. Reconstruction algorithms, including track finding and fitting in the [CDC](#) are under development and techniques to perform Particle Identification ([PID](#)) using the [StrECAL](#)

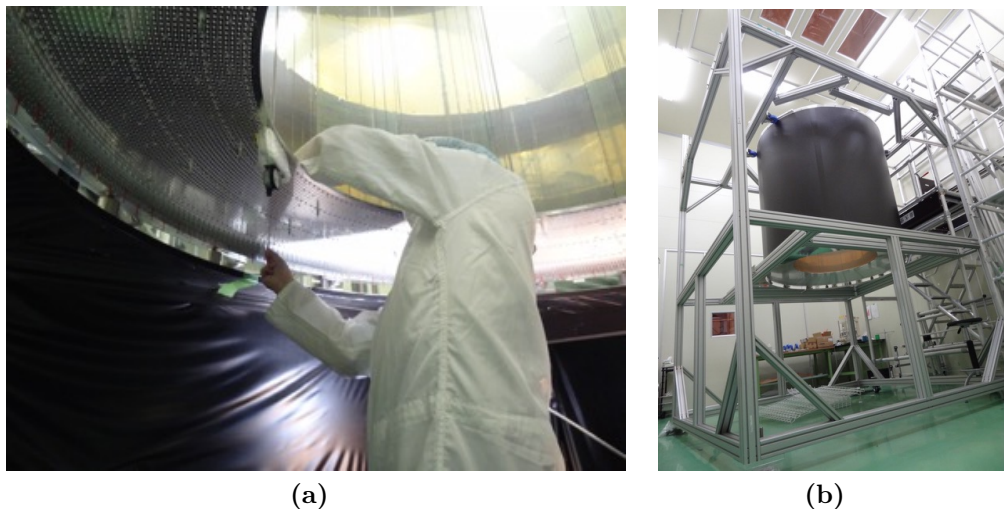


Figure 2.10.: The CDC being assembled and strung.

in the Phase-I beam are also under development. More discussion on the software and simulation can be found in the next chapter.

Chapter 3.

Offline Software and The COMET Simulation

In 2013 when I first worked on the COMET experiment, there were many disparate stand-alone simulations being run and no unified approach for data structures and analysis. Since then, a single unified software framework has been prepared and is now being used throughout the collaboration. Developing this framework has been a large part of my work over the last four years , so this chapter presents both a summary of the framework and its development as well as an explanation of the techniques used.

3.1. Developing the COMET Offline Framework

Work to produce a common, standardised software framework for COMET began when funding was awarded for Phase-I. With some four years to go before the switch on, it was clear that the support structure to handle and analyse the data needed to be in place soon. Given the scale of the project and the available resources, the decision was taken to base the COMET offline framework on an existing one, which would reduce the amount of work needed and improve the reliability of the software since it would have been tested elsewhere. A requirements document [?] was drawn up with a list of items that the software should be able to do and a survey of existing experiments undertaken to build a list of candidate frameworks. The list contained:

art A framework being developed primarily at Fermilab [18] which is also being used by Mu2e amongst other experiments.

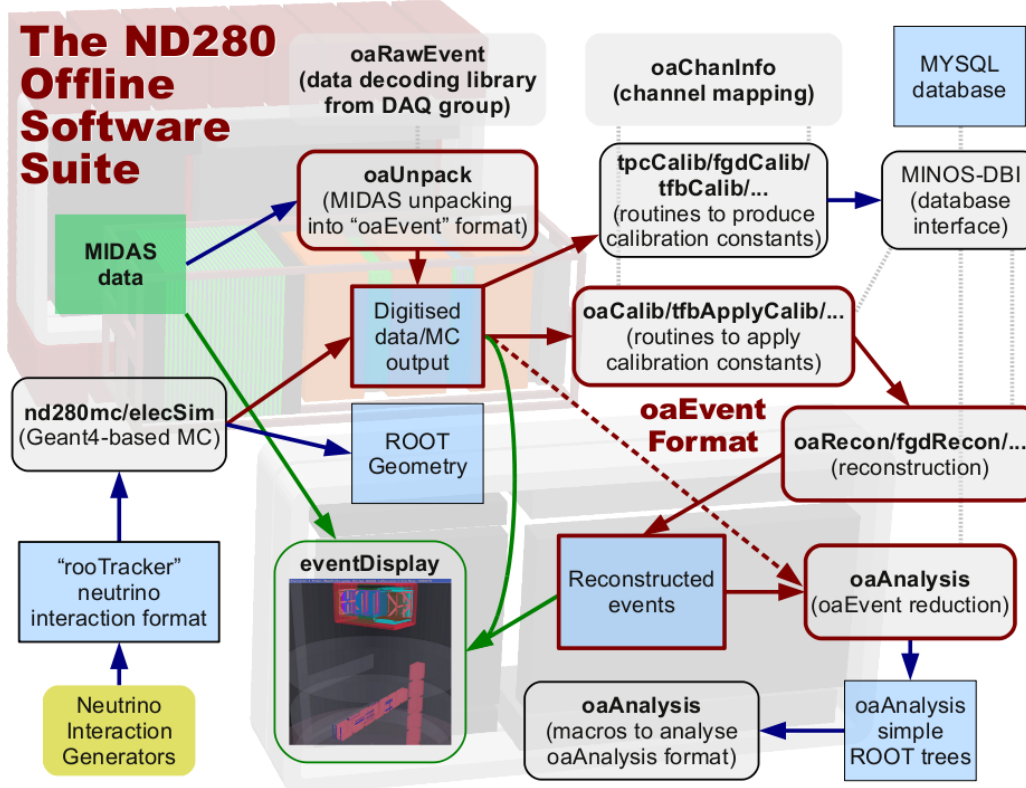


Figure 3.1.: Overview diagram for the ND280 framework.

ND280 The framework [5] used by the near detectors of the T2K experiment, which are also based at J-PARC.

GAUDI which is used by LHCb amongst other experiments [8].

MARLIN The software being developed for the International Linear Collider (ILC) [1].

The final decision was to use the ND280 framework¹ since GAUDI and MARLIN would have required too much effort to adapt to the COMET requirements; since art is used by Mu2e and keeping the software distinct is important for the two experiments to co-exist as cross-checks; and because the ND280 software was already known to a large part of the COMET collaboration and had been tested on real data at J-PARC.

Fig. 3.1 shows an overview of the ND280 framework, including its package structure and the various interactions between packages.

¹The term ‘ND280’ can refer to one of either the ND280 detector itself, the site at J-PARC that houses both the ND280 and INGRID detectors, or the software used to analyse and simulate the T2K near-detectors. For the purposes of this chapter, unless specified explicitly, the term ‘ND280’ should be taken as referring to the software.

With the decision to base the COMET experiment on the ND280 framework – and with the selection of the new name: ‘ICEDUST’ – the process of forking the software was begun. Since the ND280 framework had evolved somewhat organically a review of the conventions and code names was performed. For example, whilst the ND280 software prefixes all classes with a capital ‘T’, the ICEDUST conventions [17] agreed to swap this to a capital ‘I’ to reduce clashes with ROOT which also uses ‘T’. The package renaming scheme [?] was developed so that the purpose of a package and its role with the other packages could be more clearly identified.

Whilst fundamental, low-level packages have been left relatively unchanged higher-level packages which include more detector specific details had to be developed. Additionally some aspects of COMET needed considerably more support than had been present in the ND280 software. Some of the key changes that have been introduced between ICEDUST and ND280 are:

Simulation Although the fundamental data types have not been changed, the simulation has been nearly completely rewritten. In particular, support for hadron production codes have been added to model the production target; both the Geant4-based package (renamed to SimG4) and the detector response simulation (renamed as SimDetectorResponse) were given near-total makeovers; a new package (SimHitMerger) for resampling the G4Hits (simulated charge or energy deposits) was added. Custom physics models have been added to SimG4 to improve the modelling of the COMET-specific physics processes.

Magnetic Field handling whilst the ND280 detector has a fairly straight-forward magnetic field, the COMET experiment has anything but this. Accordingly significant work has been made to replace the way the magnetic field was handled from essentially a few constants to the ability to use complete fieldmap descriptions made with external field calculation software.

Geometry handling The unusual shape of the COMET experiment, the level of detail needed for background estimations in a high-precision experiment, and the changing nature of a staged experiment meant a more elaborate scheme for handling the geometry was necessary than had existed in ND280.

Reconstruction and Calibration packages As simply renaming of the packages, the interdependence of the calibration and reconstruction packages has been improved. Additionally, support for track fitting using Genfit2 [15] has been added as well as new track finding algorithms being developed.

In addition to the above changes to the way the software runs, the distribution of the software has changed from using CMT [2] with CVS version control to being based on git with a GitLab [11] web-based user interface for the official repository. The switch to GitLab also brought a ‘merge-request’ which has allowed development of ICEDUST to progress rapidly with only a small number of developers. Although initially the intention was also to switch the build system from CMT to CMake [3], this decision has since been reversed due to improvements in CMT.

In the 3 years since the initial work forking ND280 to produce ICEDUST in summer 2013 some 3,200 commits have edited about two million lines of code in the official version of the framework. This has been the work of some 25 collaborators whilst about 15 other users have GitLab accounts and use the software. ICEDUST has been used to run three large Monte Carlo productions, most recently simulating about 10^{11} POT events – equivalent to 18,000 Phase-I bunches – in some 100 TB of simulated data.

3.2. Overview of ICEDUST

ICEDUST Can Efficiently Do Useful Software Things and stands for the Integrated COMET Experiment Data User Software Toolkit. Fig. 3.2 shows the flow of data through the different packages of the framework and the data formats used.

Inside the framework, nearly all processing is done using a ROOT file-based format known as oaEvent. Files of this type contain header information providing run identification numbers as well as a description of the geometry and magnetic field. The data payload contained in oaEvent files is stored in a ROOT TTree with a single branch containing a single COMET event per entry. Each COMET event has a dynamic structure and can have any object which derives from the IDatum base class added to its list of data on an event-by-event basis.

Data from the detector systems is recorded in MIDAS [4] format which also contains data from the slow control monitors such as temperature sensors and high-voltage power supplies. The task of converting the MIDAS files into the oaEvent format is handled by the package oaUnpack which writes out new, converted files, and oaRawEvent which can convert the MIDAS files to oaEvent format on the fly.

Simulated data is also produced in the oaEvent format and involves some 4 to 6 packages being called, described in more depth in section 3.3.

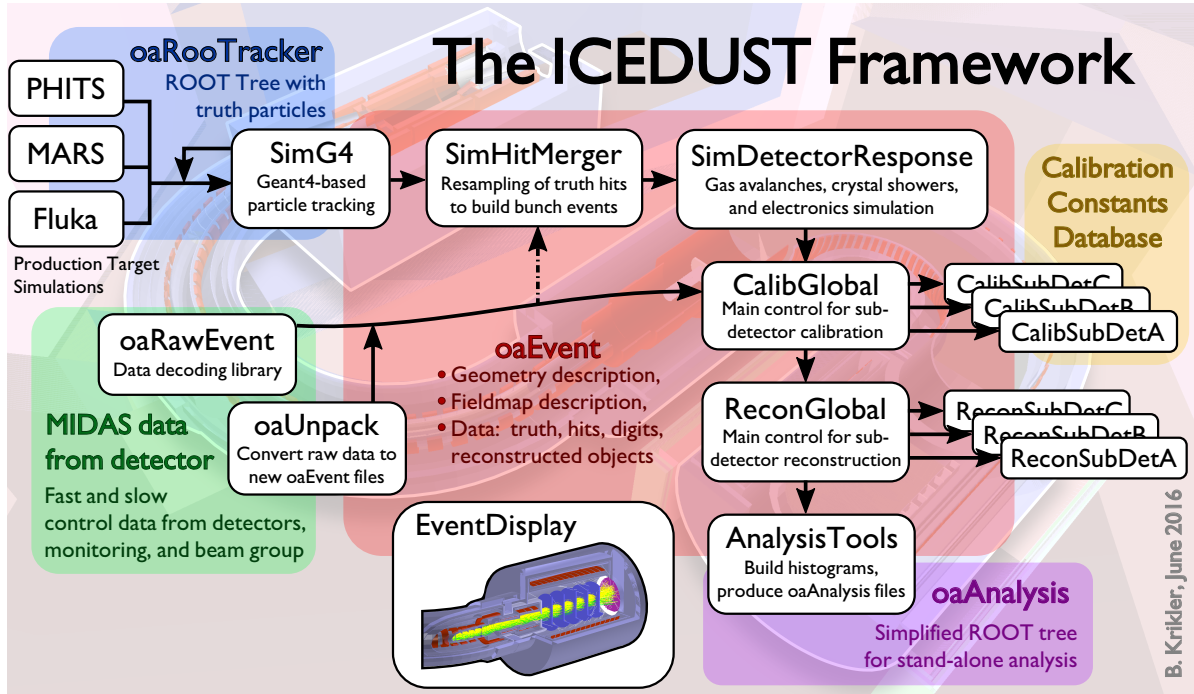


Figure 3.2.: Overview diagram for the ICEDUST framework. Data produced from simulation or taken in the real experiment are treated identically through the calibration and onwards up to analysis.

Once either simulated data has been produced or real data has been converted, calibration routines can then be applied. Each sub-detector is capable of pulling constants that were previously generated from a MySQL database and applying these to the detected (or simulated) energy deposits. These calibrated hits are then passed into the reconstruction stage. Here again each sub-detector system is first allowed to handle the data until a full reconstructed event is produced. For the tracking detectors this stage typically involves an initial track finding stage, where noise hits are removed and track candidates consisting of a list of hits are collected, and secondly a track fitting stage where the actual path of the underlying particle is reconstructed and key values like momentum and helical pitch-angle deduced.

Nearly all of the processing of data up to this stage has used the **oaEvent** format. The final analysis stage however moves into a simpler, flatter format, known as **oaAnalysis**, which produces a data summary tree (as opposed to tape) that can be accessed without a dependence on the full ICEDUST software.

Around all of this there are several utility packages, such as the event display which can visualise any oaEvent file, and IcedustControl which can run a single set of data through the data chain and is the main steering mechanism used for production running.

3.3. The COMET Simulation

The ability for an experiment to set stringent confidence limits in the event of a null-observation is determined both by the expected signal acceptance (which should be high) and the predicted number of background events (which should be low). For COMET's target single-event sensitivity – which is only a measure of the signal efficiency – to translate to a comparable confidence limit if no signal is observed, fewer than

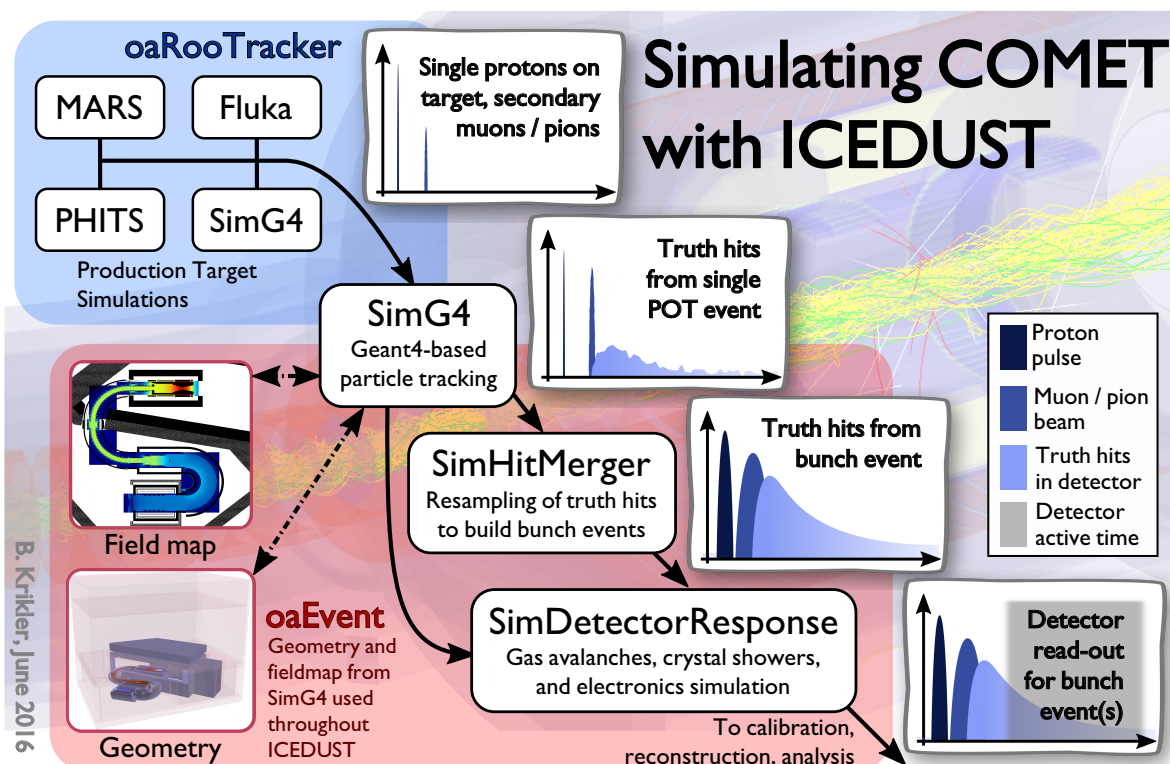


Figure 3.3.: Diagram showing the stages used to simulate COMET. The timing schematics on the right show how a simulated event is built up, firstly by producing many individual proton interactions with the production target, then by transporting the secondary particles to produce energy deposits in the detector, which are then combined with the truth hits from other proton events to produce a realistic bunch structure. Finally these bunch events are processed through the detector response simulation to produce fake waveforms and other detector read-outs.

one background events should occur during the run. By comparison, some 10^{18} and 10^{21} protons (*((CHECK: Is this the right number of protons on target?))*) will impinge the production target in Phase-I and Phase-II respectively so it is clear that the ability to suppress backgrounds must be demonstrably high.

Simulation plays a crucial role in making such a demonstration. Before the experiment is built and operated it allows one to optimise crucial aspects of the geometry and parameters, such as the magnetic field strengths or timing cuts. In addition, using Monte Carlo techniques in an accurate simulation allows an estimation of the background rate by sampling the parameter space corresponding to each stage of the experiment. Clearly then the simulation itself must be as faithful a reproduction of the true experiment as possible.

The COMET simulation therefore needs to be both highly accurate and highly efficient. As well as custom physics modelling, and special handling for the magnetic field, several resampling techniques have been introduced to increase the statistical power. The steps needed to build up the COMET simulation are shown in Fig. 3.3.

To reduce the uncertainties associated with the production target and the muon and pion yield multiple hadron codes can be used, including PHITS [16], MARS [19], Fluka [14] and Geant4 [6]. The SimG4 package, which is based on Geant4, then takes over the muon beam simulation and tracking of particles to the detectors. These energy deposits, referred to as G4Hits, can then be converted to realistic electronic detector-readouts by the SimDetectorResponse package. Often though, the G4Hits are first reshuffled with G4Hits from other events. Since one event coming out from SimG4 is

3.3.1. Handling Geometry

3.3.2. Field Calculation

3.3.3. Production Target Simulations

3.3.4. Extending the Geant4 Physics Modelling

3.3.5. Resampling With the Hit Merger

Chapter 4.

Phase-II Optimisation

1. Before a substantial sensitivity estimate can be made, need a solidly optimised design
2. Aiming for 3×10^{-17} within a single year of running
3. Designs previously optimised [?], and these results are used as nominal design / starting point
4. Fresh optimisation using new software / simulation, updated fieldmaps, physics lists and geometry
5. Some aspects fixed already since Phase-I under construction: Experiment hall, Torus1, detector solenoid, fieldmap and coil parameters?
6. Key areas for optimising:
 - 6.1. Production target dimensions
 - 6.2. Torus1 dipole field strength
 - 6.3. Torus2 dipole field strength
 - 6.4. Electron spectrometer dipole field strength
 - 6.5. collimator shapes and locations
 - 6.6. stopping target and beam blocker position and form
 - 6.7. DIO blockers on spectrometer

4.1. Optimisation Strategy

7. Take some aspects as fixed
8. Limit scope and approach:
 - 8.1. Ideally, each aspect optimised in combination to maximise signal acceptance and reduce background
 - 8.2. How decoupled are each section?
 - 8.3. In practise such an optimisation is not easy to do, instead aim to produce a baseline optimisation so that all backgrounds / issues can be identified
 - 8.4. This can then form basis for further optimisation, with perhaps a smarter more integrated approach
9. Method:
 - 9.1. Production target optimisation
 - 9.1.1. Maximise muon and pion yield between 0 and 80 MeV at entrance to muon beamline
 - 9.1.2. Parameters to vary: target length, target radius
 - 9.2. Muon beam optimisation
 - 9.2.1. Maximise muon stopping rate in stopping target
 - 9.2.2. Minimise pion stopping rate
 - 9.2.3. vary dipole along TS2 and TS4
 - 9.2.4. vary Collimators: TS2 and at TS3
 - 9.3. Electron spectrometer optimisation
 - 9.3.1. Optimise dipole to increase signal acceptance
 - 9.3.2. Optimise DIO blockers so DIO rate per straw is less than 1 kHz
 - 9.3.3. Vary solenoidal field to increase separation?
 - 9.4. Stopping target / beam blocker optimisation
 - 9.4.1. Maximise reflection of signal electrons from upstream by tuning target position

9.5. Detector optimisation

4.2. Optimisation Goals

10. Set sensitivity goal and optimise to reach this
11. Single event sensitivity only considers signal acceptance, but also need to understand backgrounds in terms of final confidence limit that can be set

4.3. Production Target Optimisation

In the Phase-II Conceptual Design Report ([CDR](#)), the production target is given as being 16 cm in length and 4 mm in radius [?]. Since then, there have been changes to the magnetic field in this region, as well as the lengths and locations of solenoids, shielding and beam-pipe, and the proton beam. Previous studies have looked at comparing the Tungsten target proposed for Phase-II to other materials [?], and also drawn a comparison between MARS [?], Geant4 [?] and the limited data available.

The goal in this study then is to optimise the production target with the up-to-date configurations. This study aims to maximise the total muon and pion yield below 80 MeV at the entrance to the Torus1 bent solenoid, by varying the radius and length of the production target.

4.3.1. Configuration

Table [4.1](#) gives the key parameters for the beam input and other aspects of this simulation. The location and orientation of the target were held fixed, since the proton beamline is fixed with respect to the muon beam axis. Once a realistic proton beam becomes available, these values would also benefit from optimisation, however. During the scan over length, the back face of the target was kept 8 cm away from the muon beam since the radiation shielding has previously been optimised, and since beyond this the magnetic field will no longer be able to capture the pions and muons produced.

It must be noted that at this point in time there is a appreciable uncertainty in the proton beam profile and position. In particular, whilst the proton beamline upstream has

Proton Beam

Horizontal spread, σ_x	5.8 mm
Vertical spread, σ_y	2.9 mm
Mean energy, μ_E	8.01 GeV
Energy spread, σ_E	0.135 MeV

Target

Material	Tungsten
Orientation	10° between target's principal axis and the muon beam axis.
Location	Back face fixed 8 cm away from muon beam axis.
Length	16 cm in CDR. Varied in steps of 4 cm from 4 to 32 cm.
Radius	4 mm in CDR. Varied from 2 to 10 cm in steps of 2 cm and from 10 to 30 cm in steps of 4 cm.

Software configuration

Packages	heads/1512w51_develop(3a0ee59)_3_UNCOMMITTED_
Externals	heads/Patch_Geant4-G4MultiLevelLocator(11fc8f0)
Fieldmap	160104 ((CHECK:))

Sample Sizes

Length scan	3e5 POT (30 runs of 1e4)
Radius scan	4.9e5 POT (49 runs of 1e4)
Final scan	

Table 4.1.: Key parameters in the configuration of the Production Target optimisation.

been well delivered, the effect of the magnetic field and necessary dipole and quadrupole magnetics are still being studied by the proton beam-line group. The beam profile is given in the Phase-I Technical Design Report ([TDR](#)) as having a Gaussian profile and energy distribution, but no divergence or location is given. The effect of the proton beam distribution on the overall sensitivity shall therefore be considered later on.

Protons originated from a plane (distributed as a two dimensional Gaussian across this surface) but since there is therefore some scope to tune the proton beam's position, the input particle plane was moved to remain 1 cm away from the front surface of the target. Since the aim is to maximise the muon and pion yield by varying only the length and radius, shifting the proton beam input plane in this way removes any variation of target acceptance due to divergences of the proton beam in the magnetic field.

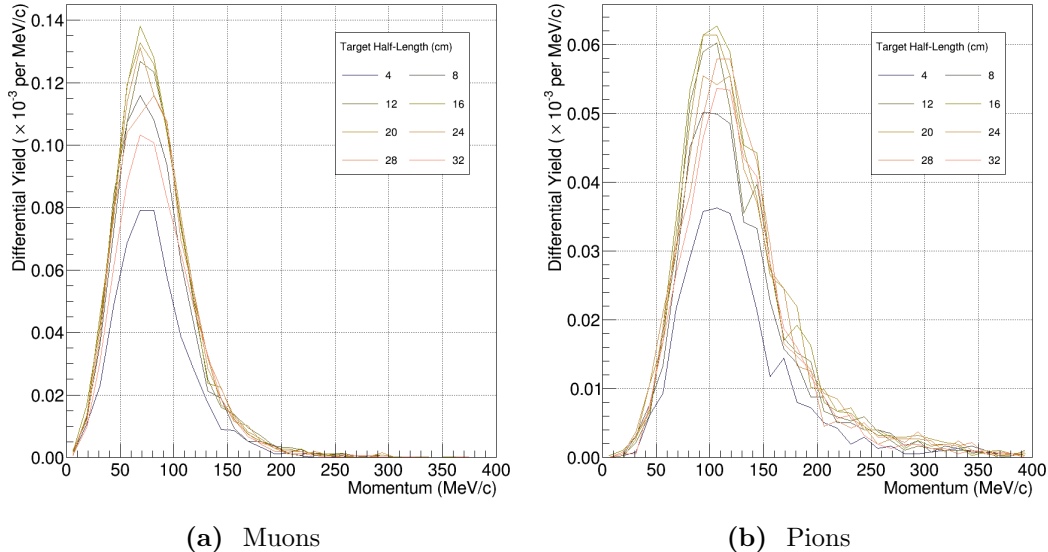


Figure 4.1.: Change to momentum distributions at the entrance to the first 90 degrees of the bent muon beam solenoid for different target lengths. Target length is given as half-length which is the Geant4 convention.

4.3.2. Length Scan

Different length targets were simulated with 3e5 POT per length. Target length was varied in steps of 4 cm from 4 to 32 cm, whilst the target radius was held fixed at the CDR value of 4 mm.

Fig. ?? shows the momentum distributions of pions and muons for different target lengths. Target length is given as half-length which is the Geant4 convention. Fig. 4.2 then shows these distributions integrated up to different momentum. From these plots it can be seen that for both muons and pions, the optimum target length occurs around a total length of 32 cm.

Additionally it can be seen from Fig. 4.3 that the shape of the momentum distributions changes only weakly as a function of the target length. These plots were produced by normalising the integrated momentum contours of Fig. 4.2 to the total integral below 400 MeV. As a result, it is possible that the actual shape variation is even weaker than apparent here, since in the present sample size, the high momentum tail is not well sampled at small target lengths, such that a skew in the normalisation might occur.

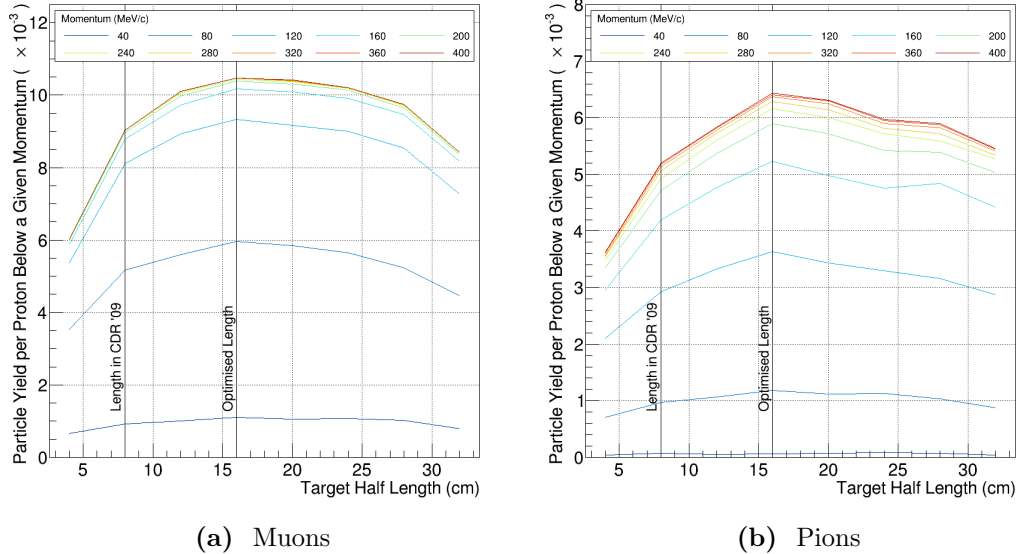


Figure 4.2.: Integrated muon and pion yields up to a certain momentum at the entrance to the first 90 degrees of the bent muon beam solenoid as a function of target length.

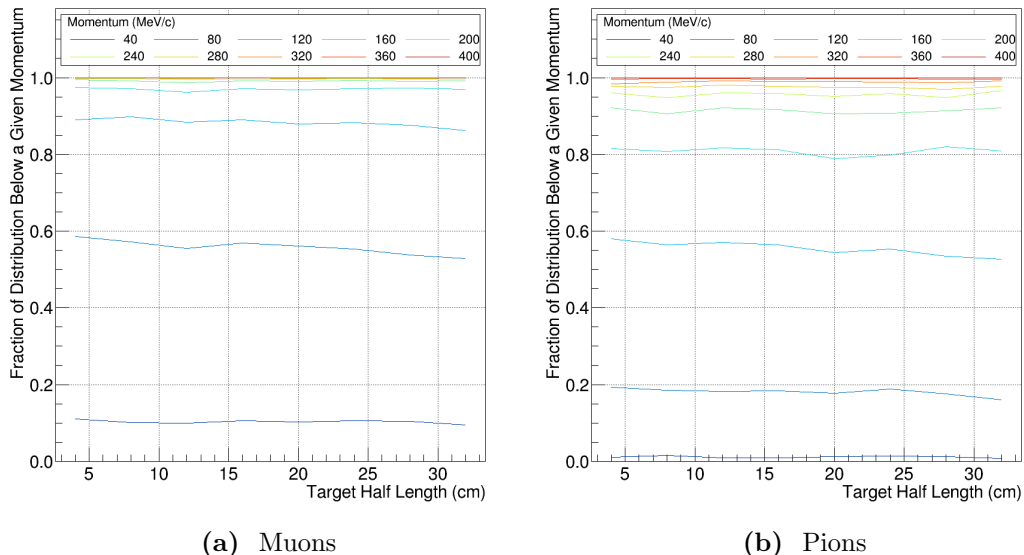


Figure 4.3.: Change in the momentum distribution of muons and pions at the entrance to the first 90 degrees of the bent muon beam solenoid as a function of target length.

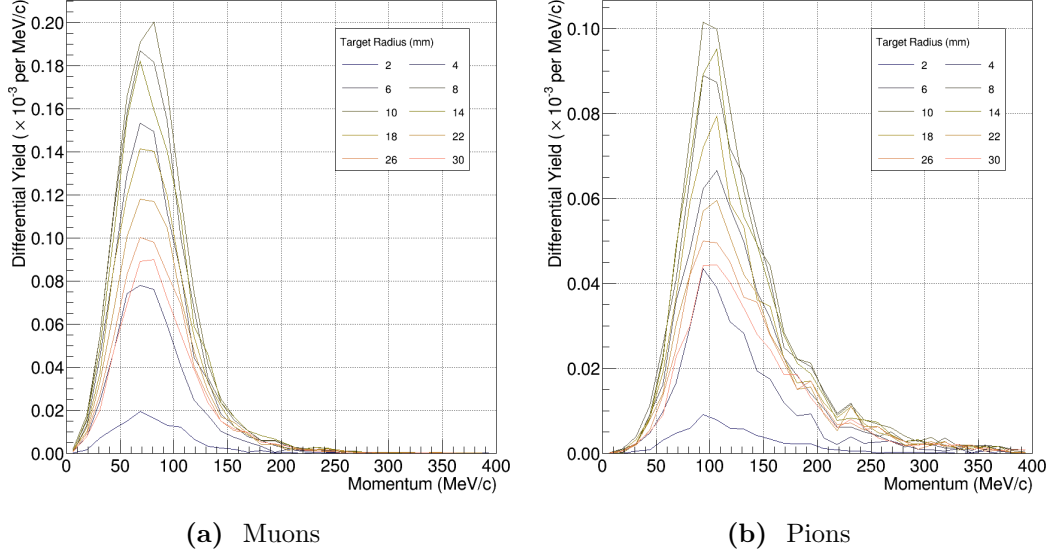


Figure 4.4.: Change to momentum distributions at the entrance to the first 90 degrees of the bent muon beam solenoid for different target radii.

4.3.3. Radius scan

In parallel to the length optimisation scan, different radii targets were also simulated. Targets with radii of 2, 4, 6, 8, 10, 14, 18, 22, 26, and 30 mm were tested. The target length was held at the [CDR](#) value of 16 cm in total.

The results of these scans can be seen in Fig. ?? and Fig. 4.5, where it can be seen that a maximum in both the muon and pion yields at the entrance to the Torus1 section is achieved at a radius of about 10 mm. As in the length scan, the shape variation of the momentum distributions is rather weak as a function of target radius.

4.3.4. Final Result

Since the length and radius scan were performed in parallel, a final cross check was performed where the optimal radius was confirmed at the optimised target length. The integrated spectrum is shown in Fig. ?? where it can be seen that the optimum radius once the target length is increased to 32 cm is still 10 mm.

12. Figure comparing Phase-II to Phase-I

13. Conclusions

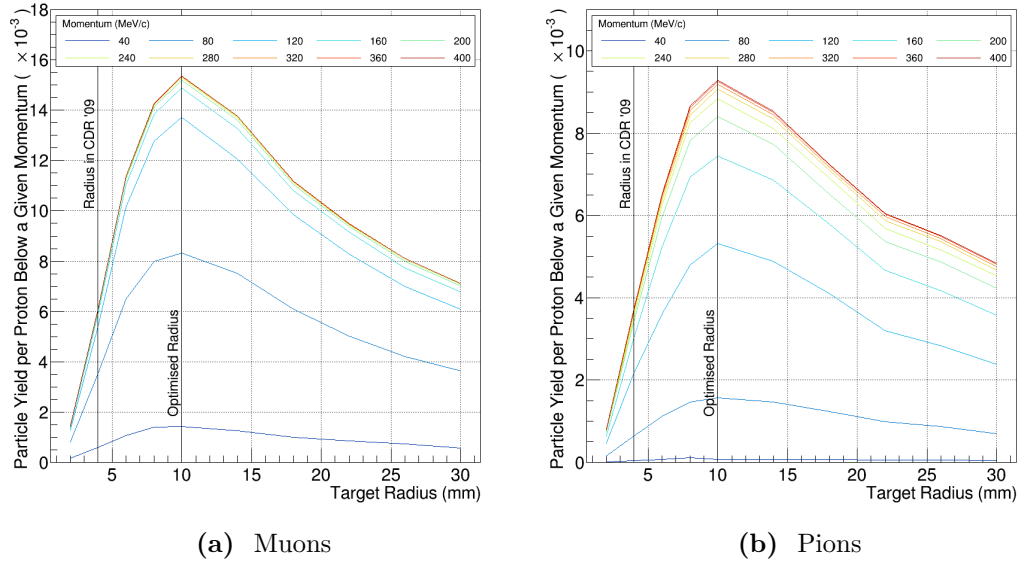


Figure 4.5.: Integrated muon and pion yields up to a certain momentum at the entrance to the first 90 degrees of the bent muon beam solenoid as a function of target radius.

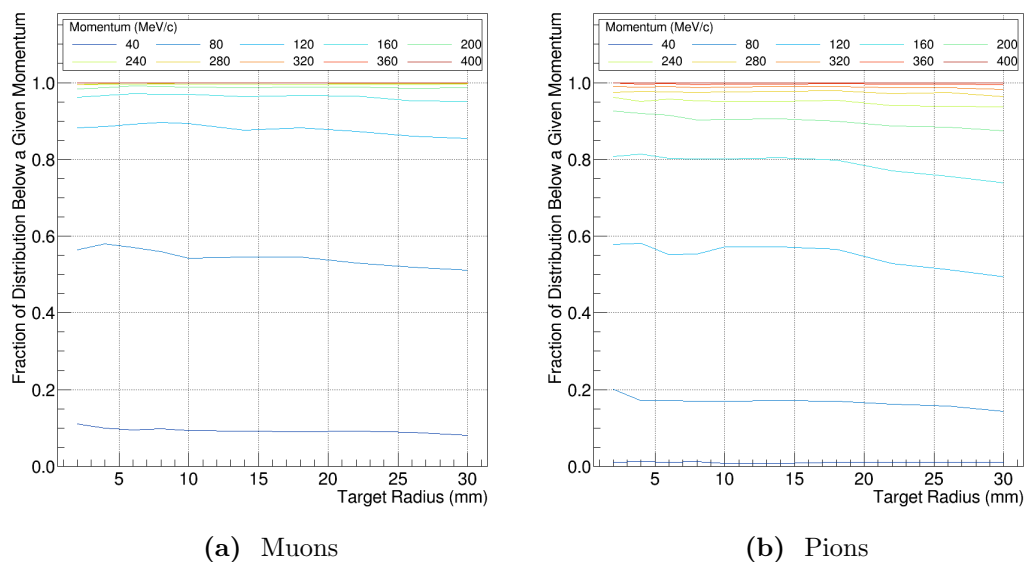


Figure 4.6.: Change in the momentum distribution of muons and pions at the entrance to the first 90 degrees of the bent muon beam solenoid as a function of target radius.

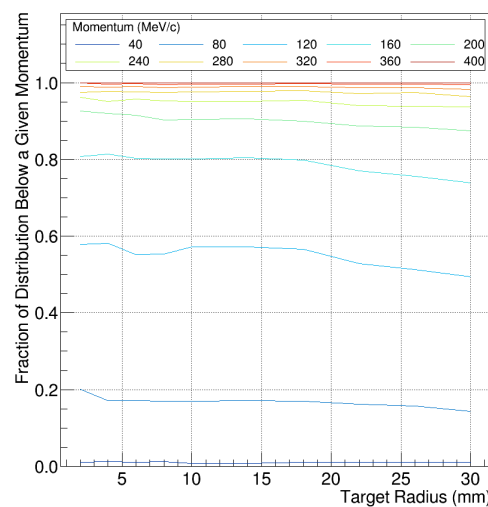


Figure 4.7.: Comparison of the combined muon and pion yield at the entrance to Torus1 for Phase-I (blue) and Phase-II (red).

Chapter 5.

Phase-II Signal Sensitivity

Chapter 6.

Phase-II Backgrounds

Appendix A.

Drifts in a Bent Solenoid

The Lorentz force:

$$\frac{d\vec{p}}{dt} = \frac{q}{m} \vec{p} \times \vec{B} \quad (\text{A.1})$$

A.1. Uniform Solenoidal Field

B field is uniform and parallel to axis of solenoid. Define the Larmor frequency, ω , and radius, a , as:

$$a = \frac{\gamma m \vec{v} \times \vec{B}}{qB^2} = \frac{p_T}{qB} \quad (\text{A.2})$$

$$\omega = \frac{qB}{m} \quad (\text{A.3})$$

A.2. Field in a Bent Solenoid

Producing a cylindrical solenoid channel can be imagined as directly bending that of a normal uniform and linear one. By symmetry it can be seen that any gradient introduced to the magnetic field can only be radially, in the plane of the bending. Further, by considering Ampere's law with a current loop in the plane of bending formed by two radial straight lines (with length $|r - R| < L$, where R and L are the bending and aperture radii of the solenoid channel) and an arc, it can be seen that the variation in

the field is given by:

$$\frac{\nabla \vec{B}}{B} = \frac{1}{r} \hat{r} \quad (\text{A.4})$$

((CHECK: Sketch or figure?))

A.3. Drift Calculation

There are two sources of drift in a bent solenoid: the gradient in the field, and the centrifugal force arising from the circular coordinate system needed to describe the field lines. The two can be treated separately in the sense that the motion of a particle moving through a field with straight field lines but with a transverse gradient given by $\nabla B/B \propto 1/r$ would be described by an equation of motion equivalent to that from the first source of drift in the bent solenoid system. Similarly, a system with a uniform field but field lines that follow circular paths would exhibit drift equivalent to the second component mentioned above.

A.3.1. Gradient Drift

“Grad-B” drift is well described in text books, but in the interest of completeness a short derivation shall be given here. The drift arising due to the gradient in the field can be treated as a perturbation of the motion of the particle in a uniform solenoidal field. The total velocity \vec{V} , is given by:

$$\vec{V} = \vec{v} + \vec{v}_g, \quad (\text{A.5})$$

where \vec{v} is the unperturbed velocity of the particle in the transverse plane, and \vec{v}_g is the velocity arising due to the gradient in the field.

Treating the field as a Taylor expansion:

$$\vec{B}(\vec{r}) = \vec{B}_0 + (\vec{r} \cdot \nabla)|_{\vec{r}=0} \vec{B} + \dots \quad (\text{A.6})$$

and substituting equations (A.5) and (A.6) into the Lorentz force, gives:

$$m \frac{d(\vec{v} + \vec{v}_g)}{dt} = q(\vec{v} + \vec{v}_g) \times \left(\vec{B}_0 + (\vec{r} \cdot \nabla)|_{\vec{r}=0} \vec{B} \right) \quad (\text{A.7})$$

$$(\text{A.8})$$

so that to first order, the perturbing velocity is given by:

$$\frac{d\vec{v}_g}{dt} = \frac{q}{m} \left(\vec{v} \times (\vec{r} \cdot \nabla)|_{\vec{r}=0} \vec{B} + \vec{v}_g \times \vec{B}_0 \right) \quad (\text{A.9})$$

Since we are only interested in steady-state solutions where \dot{v}_g is close to zero, the above equation gives:

$$\vec{v}_g = \frac{q}{m} \frac{\vec{B}_0 \times \left(\vec{v} \times (\vec{r} \cdot \nabla)|_{\vec{r}=0} \vec{B} \right)}{B_0^2} \quad (\text{A.10})$$

which by considering the form after time averaging becomes:

$$\langle \vec{v}_g \rangle_t = \frac{\vec{B}_0 \times \left(\vec{v} \times (\vec{r} \cdot \nabla)|_{\vec{r}=0} \vec{B} \right)}{B_0^2} \quad (\text{A.11})$$

List of Acronyms

CDC Cylindrical Drift Chamber

CDR Conceptual Design Report

CyDet Cylindrical Detector

DIO decay in orbit

JFY Japanese Fiscal Year

J-PARC the Japanese Proton Accelerator Research Complex

LYSO Cerium-doped Lutetium Yttrium Oxyorthosilicate

MR J-PARC Main Ring

PID Particle Identification

POT Protons on Target

RCS J-PARC Rapid Cycling Synchrotron

StrECAL Straw tube tracker and Electromagnetic Calorimeter

TDR Technical Design Report

Bibliography

- [1] see: <http://ilcsoft.desy.de/marlin>.
- [2] see: <http://www.cmtsite.org>. No longer maintained.
- [3] see: <http://www.cmake.org>.
- [4] MIDAS (Maximum Integration Data Acquisition System). <http://midas.psi.ch>. Accessed: 22-May-2015.
- [5] K. Abe, N. Abgrall, H. Aihara, Y. Ajima, J.B. Albert, and D. Allan. The t2k experiment. *Nuclear Instruments and Methods in Physics Research Section A: Accelerators, Spectrometers, Detectors and Associated Equipment*, 659(1):106 – 135, 2011.
- [6] S. Agostinelli, J. Allison, K. Amako, J. Apostolakis, H. Araujo, P. Arce, M. Asai, D. Axen, S. Banerjee, G. Barrand, F. Behner, L. Bellagamba, J. Boudreau, L. Broglia, A. Brunengo, H. Burkhardt, S. Chauvie, J. Chuma, R. Chytracek, G. Cooperman, G. Cosmo, P. Degtyarenko, A. Dell'Acqua, G. Depaola, D. Dietrich, R. Enami, A. Feliciello, C. Ferguson, H. Fesefeldt, G. Folger, F. Foppiano, A. Forti, S. Garelli, S. Giani, R. Giannitrapani, D. Gibin, J.J. Gmez Cadenas, I. Gonzlez, G. Gracia Abril, G. Greeniaus, W. Greiner, V. Grichine, A. Grossheim, S. Guatelli, P. Gumplinger, R. Hamatsu, K. Hashimoto, H. Hasui, A. Heikkinen, A. Howard, V. Ivanchenko, A. Johnson, F.W. Jones, J. Kallenbach, N. Kanaya, M. Kawabata, Y. Kawabata, M. Kawaguti, S. Kelner, P. Kent, A. Kimura, T. Kodama, R. Kokoulin, M. Kossov, H. Kurashige, E. Lamanna, T. Lampn, V. Lara, V. Lefebure, F. Lei, M. Liendl, W. Lockman, F. Longo, S. Magni, M. Maire, E. Medernach, K. Minamimoto, P. Mora de Freitas, Y. Morita, K. Murakami, M. Nagamatu, R. Nartallo, P. Nieminen, T. Nishimura, K. Ohtsubo, M. Okamura, S. O'Neale, Y. Oohata, K. Paech, J. Perl, A. Pfeiffer, M.G. Pia, F. Ranjard, A. Rybin, S. Sadilov, E. Di Salvo, G. Santin, T. Sasaki, N. Savvas, Y. Sawada, S. Scherer, S. Sei, V. Sirotenko, D. Smith, N. Starkov, H. Stoecker, J. Sulkimo, M. Takahata, S. Tanaka, E. Tcherniaev, E. Safai Tehrani, M. Tropeano, P. Truscott, H. Uno, L. Urban, P. Urban, M. Verderi, A. Walkden, W. Wander, H. Weber, J.P. Wellisch, T. Wenaus, D.C. Williams, D. Wright, T. Yamada, H. Yoshida, and D. Zschiesche. Geant4 - a simulation toolkit. *NIM in PRS A*, 506(3):250 – 303, 2003.
- [7] D. Armutliiski, Ts. Baatar, Ts. Batsaikhan, T. Kanarek, E.N. Kladnitskaya, M.U. Sultanov, R. Togoo, G.P. Toneeva, and D. Tuvdendorzh. Hadron spectra in hadron - nucleus collisions. 1991.

- [8] G. Barrand, I. Belyaev, P. Binko, M. Cattaneo, R. Chytracek, et al. GAUDI - A Software Architecture and Framework for Building HEP Data Processing Applications. *Comput.Phys.Commun.*, 140:45–55, 2001.
- [9] Wilhelm H. Bertl et al. A Search for muon to electron conversion in muonic gold. *Eur.Phys.J.*, C47:337–346, 2006.
- [10] COMET Collaboration. Conceptual design report for experimental search for lepton violating μ^-e^- conversion at sensitivity of 10^{-16} with a slow-extracted bunched proton beam (COMET), J-PARC P21.
- [11] Comet group on Gitlab. <https://gitlab.in2p3.fr/comet>.
- [12] Andrzej Czarnecki, Xavier Garcia i Tormo, and William J. Marciano. Muon decay in orbit: Spectrum of high-energy electrons. *Phys.Rev.*, D84(1):013006, 2011.
- [13] Rashid M. Djilkibaev. Meco muon yield simulation using experimental data. Technical report, Department of Physics and Astronomy, University of California.
- [14] Alfredo Ferrari, Paola R. Sala, Alberto Fasso, and Johannes Ranft. FLUKA: A multi-particle transport code (Program version 2005). 2005.
- [15] C. Hoppner, S. Neubert, B. Ketzer, and S. Paul. A Novel Generic Framework for Track Fitting in Complex Detector Systems. *Nucl. Instrum. Meth.*, A620:518–525, 2010.
- [16] H. Iwase, K. Niita, and T. Nakamura. Development of general-purpose particle and heavy ion transport monte carlo code. *Journal of Nuclear Science and Technology*, 39(11):1142–1151, 2002.
- [17] Ben Krikler, Ajit Kurup, Yoshi Uchida, Andrew Edmonds, Phill Litchfield, and the COMET Collaboration Software Group. Icedust conventions. *Internal Document*.
- [18] Robert K Kutschke. art: A framework for new, small experiments at fermilab. *Journal of Physics: Conference Series*, 331(3):032019, 2011.
- [19] Nikolai V. Mokhov. The MARS code system user’s guide version 13(95). 1995.
- [20] T. Suzuki, D. F. Measday, and J. P. Roalsvig. Total nuclear capture rates for negative muons. *Phys. Rev. C*, 35:2212–2224, Jun 1987.
- [21] The COMET Collaboration. COMET Phase-I: Technical Design Report. Technical report, KEK, April 2016.
- [22] Nam Hoai Tran. A Study of Proton Emission Following Nuclear Muon Capture for the COMET Experiment. *Thesis*, 2014.